Acta Mech 228, 1407–1413 (2017)
DOI 10.1007/s00707-016-1782-3

ORIGINAL PAPER

Yasuhide Shindo · Fumio Narita · Yuhei Goto

Cryogenic static fatigue of cracked piezoelectric ceramics in three-point bending under electric fields

Received: 9 July 2016 / Published online: 2 January 2017

Abstract This paper studies analytically and experimentally the cryogenic static fatigue behavior of cracked piezoelectric ceramics under electric fields. The crack was created normal to the poling direction. Static fatigue tests were carried out in three-point bending with the single-edge precracked-beam specimens at room temperature and liquid nitrogen temperature (77 K), and times-to-failure under different mechanical loads and electric fields were obtained. Plane strain finite element analysis using temperature-dependent material properties of piezoelectric ceramics was also performed, and the energy release rate for the permeable crack model was calculated. The effects of electric field and temperature on the energy release rate versus lifetime curve are discussed.

1 Introduction

Lead zirconate titanate (PZT) ceramics are used in special electronic devices for hydrogen applications (e.g., space and automobile) and are subjected to cryogenic temperatures [1,2]. In the application of the multilayer PZT laminates to active hydrogen fuel injectors, the laminates are also operated under electric fields at cryogenic temperatures [3,4]. On the other hand, high mechanical stresses and intense electric fields in the PZT ceramics under static and cyclic loading may cause microcracks to develop which eventually lead to failure of the devices. Hence, it is important for reliability and durability to investigate the fracture and fatigue behavior of piezoelectric ceramics at cryogenic temperatures. Recently, Shindo and Narita [5] investigated theoretically and experimentally the cryogenic fracture behavior of piezoelectric ceramics under electric fields.

It is known that electric fields can affect the fatigue life of the piezoelectric devices under sustained mechanical loading. In recent years, the effects of direct current (DC) [6] and alternating current (AC) [7] electric fields on the static fatigue behavior of cracked PZT ceramics have been investigated at room temperature (RT).

In this study, we present analytical and experimental results on the static fatigue behavior of single-edge precracked PZT ceramics under mechanical load and DC electric field at cryogenic temperatures, using three-point bending methods. The crack is created normal to the poling direction. The time-to-failure is measured as a function of mechanical load and DC electric field. Finite element analysis (FEA) was also performed, considering temperature-dependent material properties of PZT ceramics, to calculate the energy release rate for the permeable crack model. The energy release rate versus lifetime curve is then discussed.

Y. Shindo · F. Narita (✉) · Y. Goto
Department of Materials Processing, Graduate School of Engineering, Tohoku University,
Aoba-yama 6-6-02, Sendai 980-8579, Japan
E-mail: narita@material.tohoku.ac.jp
Tel.: +81-22-795-7342
Fax: +81-22-795-7342

Table 1 Material properties of C-91

	Elastic compliance ($\times 10^{-12}$ m^2/N)					Direct piezoelectric constant ($\times 10^{-12}$ m/V)			Dielectric permittivity ($\times 10^{-10}$ C/V m)	
	s_{11}	s_{33}	s_{44}	s_{12}	s_{13}	d_{31}	d_{33}	d_{15}	ϵ_{11}^T	ϵ_{33}^T
77 K	7.9	8.6	19.1	−2.91	−3.37	−118	225	291	395	490
RT	17.1	18.6	41.4	−6.3	−7.3	−340	645	836	395	490

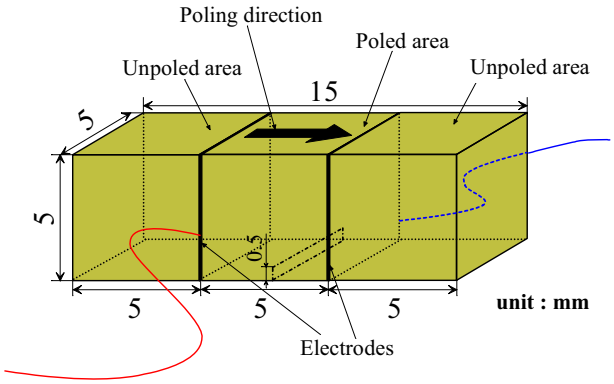

Fig. 1 SEPB specimen

2 Experimental procedure

Commercially supplied soft PZT C-91 (Fuji Ceramics Co. Ltd., Japan) was used for the experiments. The material properties are listed in Table 1, and the coercive electric field is about 0.35 MV/m. The specimen geometry is shown in Fig. 1. PZT ceramics of 5 mm × 5 mm × 5 mm were cut, and the single-edge precracked-beam (SEPB) specimen was produced by first poling a PZT and then bonding it between two unpoled PZTs by epoxy adhesive. The size of the specimens was 5 mm thick, 5 mm wide, and 15 mm long. Vickers indents were introduced using a Vickers microhardness testing machine [6], and the specimens were compressed until a precrack was formed. The crack so produced has initial length of about 0.5 mm.

Cryogenic static fatigue tests were performed under load control in servo-hydraulic testing machine (AG-50kNXplus, Shimazu Co. Ltd., Japan) using a three-point bend fixture of 13-mm loading span, and a 5-kN load cell was employed to apply the load to the SEPB specimen. Figure 2 shows the experimental setup. Time-to-failure under a constant applied load P_0 and electric field E_0 was measured at RT and 77 K. Testing at 77 K was accomplished by submerging the test fixture and specimen in liquid nitrogen. Each specimen was kept for 5 min prior to testing to ensure steady-state temperature throughout the specimen. Due to cost and time constraints, the number of specimens was limited.

3 Analysis

3.1 Basic equations

Mechanical equilibrium and Gauss' law are given by

$$\sigma_{ji,j} = 0, \tag{1}$$

$$D_{i,i} = 0, \tag{2}$$

where σ_{ij} and D_i are the components of stress tensor and electric displacement vector, and a comma denotes partial differentiation with respect to the coordinates $x_i (i = 1, 2, 3)$. We have employed Cartesian tensor notation and the summation convention for repeated tensor indices. The constitutive relation can be written as

$$\varepsilon_{ij} = s_{ijkl}\sigma_{kl} + \bar{d}_{kij}E_k, \tag{3}$$

$$D_i = \bar{d}_{ikl}\sigma_{kl} + \epsilon_{ik}^{\mathrm{T}}E_k, \tag{4}$$

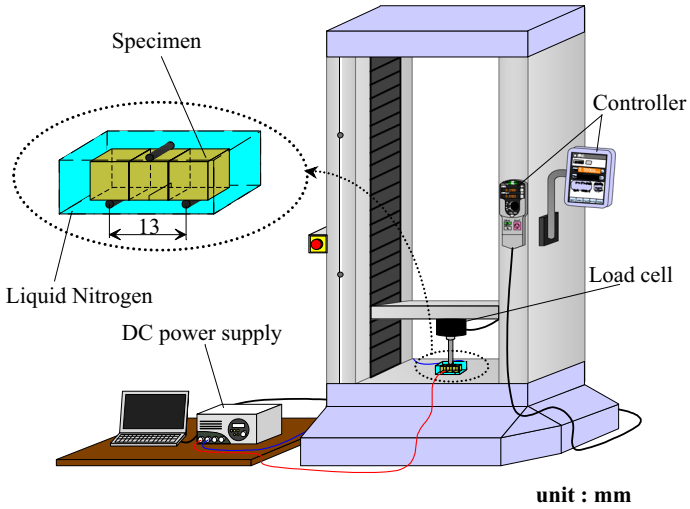

Fig. 2 Experimental setup

where ε_{ij} and E_i are the components of strain tensor and electric field intensity vector and s_{ijkl}, $\bar{d}_{kij}$, and $\epsilon^{\mathrm{T}}_{ik}$ are the elastic compliance, temperature-dependent direct piezoelectric coefficient, and permittivity at constant stress, which satisfy the following symmetry relations:

$$s_{ijkl} = s_{jikl} = s_{ijlk} = s_{klij}, \quad \bar{d}_{kij} = \bar{d}_{kji}, \quad \epsilon^{\mathrm{T}}_{ij} = \epsilon^{\mathrm{T}}_{ji}. \tag{5}$$

The strain tensor component is expressed in terms of the displacement vector component u_i by

$$\varepsilon_{ij} = \frac{1}{2}(u_{j,i} + u_{i,j}), \tag{6}$$

and the electric field intensity vector component is

$$E_i = -\phi_{,i}, \tag{7}$$

where ϕ is the electric potential. The constitutive Eqs. (3) and (4) for PZT ceramics poled in the x_3-direction are given in the Appendix. The temperature-dependent direct piezoelectric coefficient [3] is given by

$$\bar{d}_{ijk} = \begin{cases} (1.8 \times 10^{-4} T + 0.95) d_{ijk} & 192 \le T, \\ (5.5 \times 10^{-6} T^2 + 2.8 \times 10^{-3} T + 0.10) d_{ijk} & 0 < T \le 192, \end{cases} \tag{8}$$

where T is the temperature and d_{ijk} is the direct piezoelectric coefficient at 298 K.

3.2 Finite element model

Plane strain FEA was carried out for the SEPB specimen to evaluate the energy release rate G of PZT ceramics at cryogenic temperatures. The specimen and loading geometries are shown in Fig. 3. Let the coordinate axes $x = x_1$ and $z = x_3$ be chosen such that the $y = x_2$ axis coincides with the thickness direction. The z axis is the poling direction. The three-point flexure specimen with a span $S = 13$ mm is a beam of width $W = 5$ mm and length $L = 15$ mm containing a crack of length $a = 0.5$ mm. The length between two electrodes is $L_0 = 5$ mm. The specimen is subjected to a concentrated load P_0 at $x = 0, z = 0$ and a uniform electric field E_0 in the z-direction. The electric potentials of the same magnitude but opposite sign are applied at $z = \pm L_0/2$. Because of symmetry, only the right half of the model was used.

The boundary conditions at $z = 0$ can be given by

$$\begin{aligned} u_z(x, 0) &= 0 \quad (0 \le x \le W - a), \\ \sigma_{zz}(x, 0) &= 0 \quad (W - a < x \le W), \end{aligned} \tag{9}$$

$$\sigma_{zx}(x, 0) = 0 \quad (0 \le x \le W), \tag{10}$$

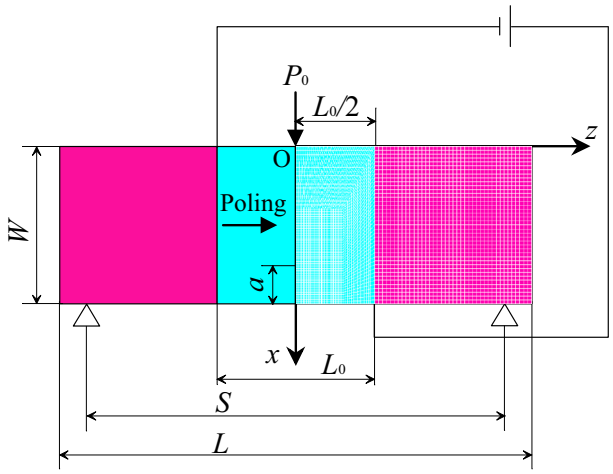

Fig. 3 Schematic representation of finite element model

$$\begin{array}{ll} \phi(x,0)=0 & (0\le x\le W-a),\\ E_x(x,0)=E_x^c(x,0) & (W-a<x\le W),\\ D_z(x,0)=D_z^c(x,0) & (W-a<x\le W), \end{array} \tag{11}$$

where the superscript c stands for the electric quantity in the void inside the crack. The electric potential is all zero on the symmetry planes inside the crack and ahead of the crack, so the boundary conditions of Eq. (11) reduce to $\phi(x,0)=0\ \ (0\le x\le W)$. Equation (11) are the permeable boundary conditions and appropriate for a slit crack in piezoelectric ceramics [8].

A mechanical load is produced by the application of a prescribed force P_0, corresponding to the appropriate experimental load, at $x=0, z=0$ along the x-direction. For an electrical load, an electric potential $\phi_0/2$ is applied at the edge $0\le x\le W, z=L_0/2$, so the condition is given by

$$\phi(x,L_0/2)=\phi_0/2\quad(0\le x\le W). \tag{12}$$

The electric field E_0 is $-\phi_0/L_0$. Other boundary conditions are summarized below.

At $z=L/2$ (side surface)

$$\sigma_{zz}(x,L/2)=0\quad(0\le x\le W), \tag{13}$$
$$\sigma_{zx}(x,L/2)=0\quad(0\le x\le W), \tag{14}$$
$$D_z(x,L/2)=0\quad(0\le x\le W). \tag{15}$$

At $x=0$ (top surface)

$$\sigma_{xx}(0,z)=-(P_0/2)\delta(z)\quad(0\le z\le L/2), \tag{16}$$
$$\sigma_{xz}(0,z)=0\quad(0\le z\le L/2), \tag{17}$$
$$D_x(0,z)=0\quad(0\le z\le L/2). \tag{18}$$

At $x=W$ (bottom surface)

$$\sigma_{xx}(W,z)=0\quad(0\le z<S/2, S/2<z\le L/2),\quad u_x(W,S/2)=0, \tag{19}$$
$$\sigma_{xz}(W,z)=0\quad(0\le z\le L/2), \tag{20}$$
$$D_x(W,z)=0\quad(0\le z\le L/2). \tag{21}$$

In Eq. (16), $\delta(z)$ is the Dirac delta function.

The energy release rate was computed using the path-independent integral approach. The energy release rate G is given by

$$\begin{aligned} G=\int_{\Gamma_0}\{&Hn_x-(\sigma_{xx}u_{x,x}+\sigma_{zx}u_{z,x})n_x-(\sigma_{zx}u_{x,x}+\sigma_{zz}u_{z,x})n_z\\ &+D_xE_xn_x+D_zE_xn_z\}\mathrm{d}\Gamma, \end{aligned} \tag{22}$$

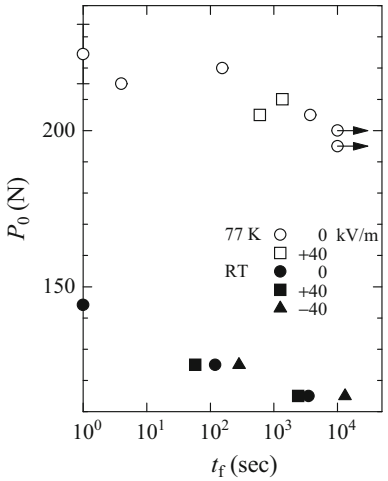

Fig. 4 Static fatigue curves of PZT C-91 ceramics at RT and 77 K

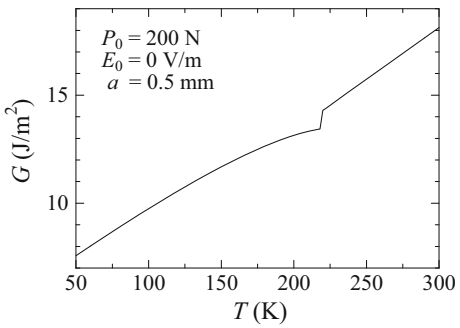

Fig. 5 Energy release rate versus temperature

where H is the electrical enthalpy density, Γ_0 is the contour closing a crack tip, and n_x, n_z are the components of the outer unit normal vector.

The temperature-dependent direct piezoelectric coefficient, Eq. (8), was used. In the elastic compliance s_{33} of C-91 at 77 K, the measured value by a compression test [9] was about 8.6×10^{12} m^2/N. Here, the elastic compliance s_{33} was assumed to have a linear relationship with temperature T between RT and 77 K [10], and the other elastic compliances $s_{11}, s_{12}, s_{13}, s_{44}$ were presumed to have the same temperature dependence. For simplicity, the permittivities $\epsilon_{11}^{\mathrm{T}}, \epsilon_{33}^{\mathrm{T}}$ of C-91 were assumed to be independent of temperature. Making use of temperature-dependent piezoelectric coefficients d_{33}, d_{31}, d_{15} and elastic compliances $s_{11}, s_{33}, s_{12}, s_{13}, s_{44}$, the model calculates the temperature-dependent energy release rate G.

For the calculation of the energy release rate G, three contours were defined in the finite element mesh. The values of G for each of these contours are practically identical and the variations with respect to the average value of G from three contours are less than 2%. Four-node element PLANE 13 in ANSYS was used. The finite element mesh had 2250 elements and 2346 nodes.

4 Results and discussion

Figure 4 shows the static fatigue curves of PZT ceramics at RT and 77 K. The fracture test results (average of four measurements without electric field) on PZT ceramics are also shown. At RT, times-to-failure of PZT ceramics under electric fields, 40 and −40 kV/m, are lower and higher than under 0 V/m, respectively. Similarly, at cryogenic temperatures, a positive electric field decreases the times-to-failure. Figure 5 shows the FEA result for the energy release rate G versus temperature T for C-91 ceramics with a permeable crack of length $a = 0.5$ mm under load $P_0 = 200$ N and electric field $E_0 = 0$ V/m. The value of G decreases as the temperature decreases. One reason for this are the temperature-dependent direct piezoelectric coefficients due

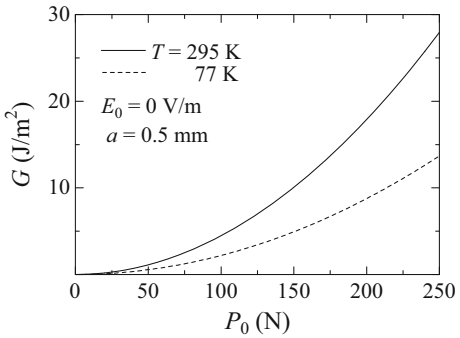

Fig. 6 Energy release rate versus mechanical load

to a shift in the morphotropic phase boundary (MPB) between the tetragonal and rhombohedral/monoclinic phases [3], i.e., tetragonal to monoclinic phase transformation. Another reason is attributed to the temperature-dependent elastic compliances. Therefore, the fracture load at 77 K is larger than that at RT (value of P_0 at 10^0 s in Fig. 4). Figure 6 shows the energy release rate versus mechanical load P_0 for C-91 ceramics with $a = 0.5$ mm under $E_0 = 0$ V/m. The dashed line represents the value of G at 77 K, and the solid line denotes G at 295 K (RT). The energy release rate increases nonlinearly with increasing mechanical load. The increase in G contributes to the decrease in the time-to-failure at RT and 77 K.

5 Conclusions

Static fatigue of cracked piezoelectric ceramics under electric fields at cryogenic temperatures was studied, using a three-point bending technique, analytically and experimentally. It was found that the time-to-failure under a positive electric field was shorter than that under no electric field at RT and 77 K. Also, under zero electric field, the fracture load at 77 K was larger than that at RT, and with decreasing in temperature, the energy release rate decreased.

Appendix A

For piezoelectric ceramics which exhibit symmetry of a hexagonal crystal of class 6mm with respect to principal x_1, x_2, and x_3 (poling) axes, the constitutive relations can be written in the following form:

$$\begin{Bmatrix} \varepsilon_{11} \\ \varepsilon_{22} \\ \varepsilon_{33} \\ 2\varepsilon_{23} \\ 2\varepsilon_{31} \\ 2\varepsilon_{12} \end{Bmatrix} = \begin{bmatrix} s_{11} & s_{12} & s_{13} & 0 & 0 & 0 \\ s_{12} & s_{11} & s_{13} & 0 & 0 & 0 \\ s_{13} & s_{13} & s_{33} & 0 & 0 & 0 \\ 0 & 0 & 0 & s_{44} & 0 & 0 \\ 0 & 0 & 0 & 0 & s_{44} & 0 \\ 0 & 0 & 0 & 0 & 0 & s_{66} \end{bmatrix} \begin{Bmatrix} \sigma_{11} \\ \sigma_{22} \\ \sigma_{33} \\ \sigma_{23} \\ \sigma_{31} \\ \sigma_{12} \end{Bmatrix} + \begin{bmatrix} 0 & 0 & \bar{d}_{31} \\ 0 & 0 & \bar{d}_{31} \\ 0 & 0 & \bar{d}_{33} \\ 0 & \bar{d}_{15} & 0 \\ \bar{d}_{15} & 0 & 0 \\ 0 & 0 & 0 \end{bmatrix} \begin{Bmatrix} E_1 \\ E_2 \\ E_3 \end{Bmatrix}, \tag{23}$$

$$\begin{Bmatrix} D_1 \\ D_2 \\ D_3 \end{Bmatrix} = \begin{bmatrix} 0 & 0 & 0 & 0 & \bar{d}_{15} & 0 \\ 0 & 0 & 0 & \bar{d}_{15} & 0 & 0 \\ \bar{d}_{31} & \bar{d}_{31} & \bar{d}_{33} & 0 & 0 & 0 \end{bmatrix} \begin{Bmatrix} \sigma_{11} \\ \sigma_{22} \\ \sigma_{33} \\ \sigma_{23} \\ \sigma_{31} \\ \sigma_{12} \end{Bmatrix} + \begin{bmatrix} \epsilon_{11}^{\mathrm{T}} & 0 & 0 \\ 0 & \epsilon_{11}^{\mathrm{T}} & 0 \\ 0 & 0 & \epsilon_{33}^{\mathrm{T}} \end{bmatrix} \begin{Bmatrix} E_1 \\ E_2 \\ E_3 \end{Bmatrix}, \tag{24}$$

where

$$\sigma_{23} = \sigma_{32}, \quad \sigma_{31} = \sigma_{13}, \quad \sigma_{12} = \sigma_{21}, \tag{25}$$

$$\varepsilon_{23} = \varepsilon_{32}, \quad \varepsilon_{31} = \varepsilon_{13}, \quad \varepsilon_{12} = \varepsilon_{21}, \tag{26}$$

$$\left.\begin{array}{l} s_{11} = s_{1111} = s_{2222}, \quad s_{12} = s_{1122}, \quad s_{13} = s_{1133} = s_{2233}, \quad s_{33} = s_{3333}, \\ s_{44} = 4s_{2323} = 4s_{3131}, \quad s_{66} = 4s_{1212} = 2(s_{11} - s_{12}), \end{array}\right\} \tag{27}$$

$$\bar{d}_{15} = 2\bar{d}_{131} = 2\bar{d}_{223}, \quad \bar{d}_{31} = \bar{d}_{311} = \bar{d}_{322}, \quad \bar{d}_{33} = \bar{d}_{333}. \tag{28}$$

References

1. Qing, X.P., Beard, S.J., Kumar, A., Sullivan, K., Aguilar, R., Merchant, M., Taniguchi, M.: The performance of a piezoelectric-sensor-based SHM system under a combined cryogenic temperature and vibration environment. Smart Mater. Struct. **17**, 055010 (2008)
2. Park, J.M., Taylor, R.P., Evans, A.T., Brosten, T.R., Nellis, G.F., Klein, S.A., Feller, J.R., Salerno, L., Gianchandani, Y.B.: A piezoelectric microvalve for cryogenic applications. J. Micromech. Microeng. **18**, 015023 (2008)
3. Shindo, Y., Narita, F., Sasakura, T.: Cryogenic electromechanical behavior of multilayer piezo-actuators for fuel injector applications. J. Appl. Phys. **110**(8), 084510 (2011)
4. Shindo, Y., Sasakura, T., Narita, F.: Dynamic electromechanical response of multilayered piezoelectric composites from room to cryogenic temperatures for fuel injector applications. ASME J. Eng. Mater. Technol. **134**(3), 031007 (2012)
5. Shindo, Y., Narita, F.: Cryogenic fracture of cracked piezoelectric ceramics in three-point bending under electric fields. Acta Mech. **225**(4/5), 1313–1321 (2014)
6. Shindo, Y., Narita, F., Saito, F.: Static fatigue behavior of cracked piezoelectric ceramics in three-point bending under electric fields. J. Eur. Ceram. Soc. **27**(10), 3135–3140 (2007)
7. Shindo, Y., Narita, F., Morikawa, Y.: Static fatigue of three-point bending piezoelectric ceramics with a single-edge crack under AC electric fields. J. Am. Ceram. Soc. **95**(4), 1326–1332 (2012)
8. Shindo, Y., Narita, F., Hirama, M.: Effect of the electrical boundary condition at the crack face on the mode I energy release rate in piezoelectric ceramics. Appl. Phys. Lett. **94**(8), 081902 (2009)
9. Shindo, Y., Watanabe, S., Takeda, T., Miura, M., Narita, F.: Controllability of cryogenic mode I delamination behavior in woven fabric composites using piezoelectric actuators. Eng. Fract. Mech. **102**, 171–179 (2013)
10. Sabat, R.G., Mukherjee, B.K., Ren, W., Yang, G.: Temperature dependence of the complete material coefficients matrix of soft and hard doped piezoelectric lead zirconate titanate ceramics. J. Appl. Phys. **101**(6), 064111 (2007)